Sports Eng (2009) 12:31–40
DOI 10.1007/s12283-009-0026-3

ORIGINAL ARTICLE

Numerical modelling of rowing blade hydrodynamics

Andrew Sliasas · Stephen Tullis

Published online: 10 September 2009
© International Sports Engineering Association 2009

Abstract The highly unsteady flow around a rowing blade in motion is examined using a three-dimensional computational fluid dynamics (CFD) model which accounts for the interaction of the blade with the free surface of the water. The model is validated using previous experimental results for quarter-scale blades held stationary near the surface in a water flume. Steady-state drag and lift coefficients from the quarter-scale blade flume simulation are compared to those from a simulation of the more realistic case of a full-scale blade in open water. The model is then modified to accommodate blade motion by simulating the unsteady motion of the rowing shell moving through the water, and the sweep of the oar blade with respect to the shell. Qualitatively, the motion of the free surface around the blade during a stroke shows a realistic agreement with the actual deformation encountered during rowing. Drag and lift coefficients calculated for the blade during a stroke show that the transient hydrodynamic behaviour of the blade in motion differs substantially from the stationary case.

Keywords Rowing · Blade · Hydrodynamics · Lift · Drag

1 Introduction

To date, there have not been any comprehensive fluid dynamic investigations performed on a rowing blade under realistic rowing conditions. A study of this nature would elucidate the unsteady flow behaviour around a rowing blade in motion, allowing investigation into areas for optimisation. Although blade shapes have evolved through the years, all innovations have been based and tested on a qualitative assessment of what would constitute an effective design. The potential for blade design improvements stemming from an improved knowledge of blade hydrodynamics, then, should be considered great [1].

The interaction of the oar, the rower and the water during a stroke behaves as a lever. At the beginning of a stroke, known as the *catch*, the rower inserts the blade in the water and pries the shell forward by pulling on the oar handle, levering the shell about the blade. At the end of the stroke, the *finish*, the blade is extracted from the water and the shell glides forward while the rower moves into position for the next stroke. From catch to finish the blade moves minimally longitudinal to the shell direction, remaining essentially locked in a pocket of water (Fig. 1).

The blade–water interaction is not straightforward, however. Over the duration of the stroke while the blade is in the water, the angle of attack (the angle of the direction of flow onto the blade chord line), α, varies considerably and drastically in less than a second [2]. At the beginning of the stroke the flow is nearly collinear with the blade chord line ($\alpha \approx 0$), and in less than a second, α rapidly sweeps an arc of over 190° across the blade. In addition to a drag force acting collinear with the flow on the blade, Nolte [3] argues that near the catch the blade acts as a hydrofoil, with a lift force perpendicular to the flow direction contributing significantly to propulsion. The flow around the blade is further complicated by the surface of the water. The position of the blade, buried just below the water for the duration of the stroke, deforms the water surface creating a bulge over and depression behind the blade. The highly unsteady nature of this flow, combined

A. Sliasas (✉) · S. Tullis
Department of Mechanical Engineering, McMaster University, 1280 Main St. W., Ontario L8S 4L8, Canada
e-mail: sliasaae@mcmaster.ca

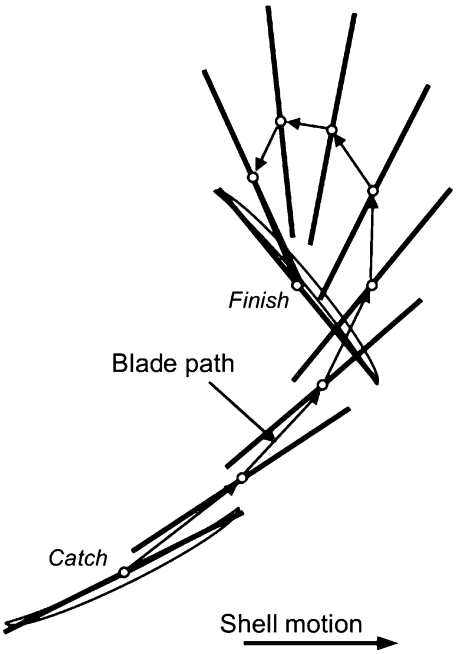

Fig. 1 Approximate path of the blade centre through the water during the stroke. The shell motion is from left to right (Adapted with permission from Kleshnev [15])

with its strongly three-dimensional character, makes studying its dynamic character very challenging.

The difficulty in obtaining pertinent data is one reason why little attention has been given to data-based hydrodynamic studies of blade shape design. An experimental apparatus that can replicate the blade motion through the water caused by an accelerating shell is very difficult to create. Combined with the challenge of acquiring data relating to the flow about the blade from such experiments and the time-intensive process of creating physical blades to be tested, this method of flow study has not been fruitful. Experiments performed under actual rowing conditions have, however, been able to successfully extract certain quantitative rowing data. By fitting rowing equipment with sensors, such setups could record force data applied at the oar handle, the angular position of the oar and the velocity of the shell during the stroke [4]. The problem with this experimental method is that it is highly unrepeatable as each individual stroke is strongly dependent on externalities (the rower, water conditions, etc.) As well, the inclusion of sensors and instrumentation alters the delicate balance of the shell. These experiments, however, provide information as to how the velocity of the shell and rotation of the oar through a stroke are linked.

Other attempts to study the blade quantitatively focused on steady-state experiments, such as those of Caplan and Gardner [5, 6]. In their experiments, a curved rectangular plate with the same curvature and projected surface area as a standard hatchet blade was held fixed in a flume as water was forced past [6]. Sensors on the oar shaft were used to resolve the force of the water on the blade, which allowed drag and lift coefficients to be calculated. While these experiments benefited from being conducted in a controlled laboratory setting, they did not capture the unsteady flow effects associated with a blade in motion, which should be considered important [2].

Applying computational fluid dynamics (CFD) to complex flow situations like that of the flow about a rowing blade is now feasible thanks to affordable computing resources. Leroyer et al. [7] created a numerical simulation for a blade in motion near a free surface and performed experiments to validate their results. In their work, they used a frame of reference of the earth and moved the blade through a prescribed motion. The trajectory of the blade was based on a varying oar rotation rate and a constant shell velocity. This produced a symmetric path through the water, following essentially a prolate cycloid pattern. Although experimental and numerical data matched well, their results did not account for an accelerating shell velocity coupled with the oar rotation rate.

The aim of this paper is to outline the development of a CFD simulation which accurately replicates the hydrodynamic behaviour of a rowing stroke. An initial flow simulation reproduces the steady-state experiments of a quarter-scale blade in a water flume performed by Caplan and Gardner [6], allowing validation of the CFD model. The model blade is then enlarged to fullscale, and steady-state flow characteristics in open water conditions are compared to those at quarter-scale within the flume. Finally, the computational model is modified to incorporate the unsteady transient effects of a blade in motion based on a frame of reference of an accelerating shell. Results from this unsteady flow simulation are analysed and compared to steady-state conditions.

2 Numerical model validation

As the first step in creating a numerical simulation of the rowing stroke, the experimental configuration of Caplan and Gardner [6] was modelled using CFD. The ability of the simulation to accurately replicate their experimental results would verify the validity of the numerical model. In their experiments, a quarter-scale curved rectangular blade was held fixed in a water flume, with the top edge of the blade flush with the surface of the water. Average force measurements were obtained using strain gauges located on the shaft holding the blade. The steady-state experiments were run with the blade held at α values ranging from 0° to 180° in 5° increments.

The domain of the model in the present simulation, which matches experimental conditions [6], can be seen

in Fig. 2. Table 1 outlines relevant dimensions of the blade and water flume. The length of the flume was such that upstream and downstream conditions were uniform at the inlet and outlet boundaries. At the inlet, a water velocity of 0.75 m s^{-1} was specified, as in the experiment. At the outlet, a zero relative static pressure boundary condition was imposed. The side walls and bottom surface of the flume were modelled as no-slip surfaces. The top surface was modelled as a zero relative static pressure opening with no velocity gradient perpendicular to the boundary.

The proximity of the blade to the water surface meant that free surface conditions would be important for the simulation. A multiphase flow with the top edge of the blade positioned flush with the water surface and a region of air above accomplished this. To define the multiphase flow, a volume of fluid (VOF) method was used [8]. With this approach, the volume fraction of fluid in each domain element, φ, is tracked throughout the solution stage. Most domain elements are comprised entirely of water ($\varphi_{water} = 0$) or air ($\varphi_{air} = 1$). Elements at the free surface, where the interface divides an element, have fractional φ values ($0 < \varphi < 1$). The shape of the free surface is constructed in a piecewise manner based on the volume fractions of individual elements [9]. The VOF method treats the entire flow field as homogeneous, with common transported velocity and pressure quantities for all fluid phases.

The flow was solved using the three-dimensional unsteady turbulent Navier–Stokes equations modified to account for multiphase flow. These transport equations are similar to those for a single-phase flow, but incorporate the different density and dynamic viscosity values of each fluid phase. Assuming volume conservation within each domain element,

$$\varphi_{water} + \varphi_{air} \equiv 1 \tag{1}$$

and that transported velocity and pressure quantities are the same across each fluid phase, the conservation of mass equations for the water and air phases are, respectively,

Table 1 Dimensions of the flume and blade for the quarter-scale steady-state simulations

Blade	
Width	12.56 cm
Depth	6.25 cm
Projected area	78.5 cm^2
Thickness	1.80 mm
Flume	
Width	64.0 cm
Length	128.0 cm
Depth	15.0 cm (+20.0 cm of air above)

$$\frac{\partial}{\partial t}(\varphi_{water}\rho_{water}) + \frac{\partial}{\partial x_i}(\varphi_{water}\rho_{water}u_i) = 0 \tag{2}$$

$$\frac{\partial}{\partial t}(\varphi_{air}\rho_{air}) + \frac{\partial}{\partial x_i}(\varphi_{air}\rho_{air}u_i) = 0 \tag{3}$$

The momentum equations are defined as,

$$\frac{\partial}{\partial t}(\rho u_j) + u_i\frac{\partial}{\partial x_i}(\rho u_j) = -\frac{\partial p}{\partial x_j} + (\mu + \mu_t)\frac{\partial^2 u_j}{\partial x_i^2} \tag{4}$$

where u_i is the velocity in the x-direction, p is the pressure, and μ_t is the turbulence viscosity. Density (ρ) and dynamic viscosity (μ) are volume averages of the properties of each phase,

$$\rho = \varphi_{water}\rho_{water} + \varphi_{air}\rho_{air} \tag{5}$$

$$\mu = \varphi_{water}\mu_{water} + \varphi_{air}\mu_{air} \tag{6}$$

Turbulent flow effects were modelled using a shear stress transport (SST) model [10]. The SST model was chosen for its ability to accurately predict the onset and amount of flow separation from a foil in an adverse pressure gradient [11]. The SST model blends the k-ε model which is quite stable for free-shear flows with the k-ω model which is better suited for near-wall flow. Transport effects, which are also important for predicting adverse pressure gradient flows, are included in the eddy viscosity formulation in the SST model. The turbulence

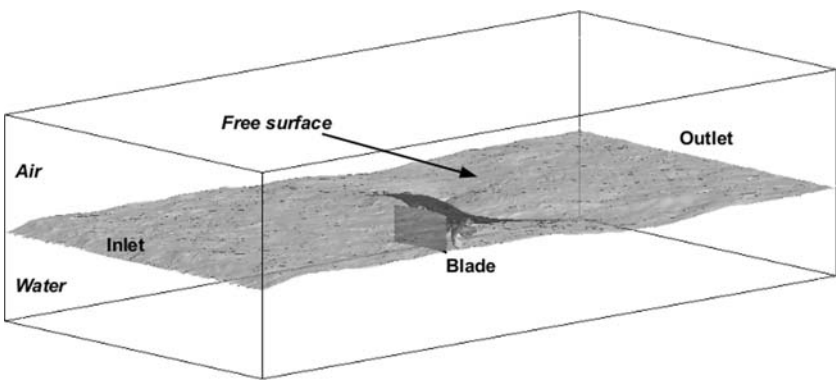

Fig. 2 Domain for the steady-state quarter-scale blade simulations. Fluid flows in the left, around the blade, and exits at the right. The side and bottom surfaces are no-slip walls, and the top surface is a zero-pressure gradient opening. The steady-state free surface is indicated

intensity at the inlet, defined as the ratio of turbulent velocity fluctuations to the mean flow velocity ($I = u'/U$), was specified at 5%. The turbulence length scale was set to the depth of the water (15 cm).

An unstructured tetrahedral mesh for the domain was generated using ANSYS CFX-Mesh. A maximum element edge length of 4 cm was used away from the blade in the bulk flow region. To capture the detail of the flow around the blade, a maximum element edge length of 0.5 cm was applied on the blade surfaces. In addition, a 1.8 mm thick set of boundary layer cells was included adjacent to the blade and at the flume walls to resolve the no-slip condition. To keep a sharp interface at the air and water boundary, three successive mesh refinements were performed during the solution stage. For each refinement, the size of the elements near the free surface was halved, thereby increasing the mesh resolution along the free surface. A grid test was performed, and a 740,000 element domain mesh yielded grid-independent results, having less than a 1% difference in the resultant steady-state blade forces when compared to a 370,000 element mesh.

A timestep independence test indicated that a 0.005 s time interval resolved the time dependencies of the flow. Using the ANSYS CFX commercial CFD code, the governing equations were solved at each timestep until the root mean square residuals of the mass and momentum conservation equations fell below 10^{-4}. The simulation was run for 5 s, and the monitored blade forces reached steady-state conditions. Simulations were repeated for α ranging from 0° to 180° at 15° increments. After solving the flow using the SST model, the simulations were run again using the standard two-equation k-ε model [12] with the same turbulence intensity and length scale as a basis for comparison. When blade force data produced by the two simulations were compared, the results were in very close agreement. Although the flow separates at the leading edge of the blade for angles of attack close to 90°, the k-ε model predicts forces on the blade within 1% of the results from the SST model. For the purposes of this study, both turbulence models resolve the flow about the blade well enough to provide an accurate resultant force on the blade. Results generated using the SST model were used to calculate drag and lift coefficients at each angle (Fig. 3).

As seen in Fig. 3, the drag and lift coefficients from the simulations match very well with those from the experiments. The simulated coefficients are slightly lower ($\sim$10%) than the experimental values, however, which is most pronounced near the peaks of the curves. It is noted that in Caplan and Gardner's experiments [6], due to the way in which the support shaft was connected to the blade, part of the shaft was below the water surface. It would be expected that this increased surface area of the blade apparatus exposed to the flow would lead to an overestimation of the experimental drag and lift coefficients. The ability of the present simulation to replicate the quarter-scale experimental results validates the numerical model, providing confidence in its ability to handle similar flows.

3 Full-scale steady flow simulation

The next step in the present investigation involves a steady flow analysis for a full-scale blade in realistic open water conditions. These results will be used for comparison with the unsteady flow of a blade in motion, because there is evidence that the quarter-scale blade drag and lift characteristics determined by Caplan and Gardner [6] are scale-dependent. Although a flume velocity greater than 0.7 m s^{-1} was stated to be Reynolds number independent [5], research by Coppel et al. [13, 14] found that the 0.75 m s^{-1} flume velocity was not in fact within the range of Reynolds number independence. In their study, numerical simulations of both the quarter-scale blade flume experiments of Caplan and Gardner and of a full-scale blade in a geometrically similar (four times larger) flume were performed, modelling the water surface as a symmetry plane. A comparison of drag and lift coefficients from both simulations revealed that although lift characteristics at both scales were similar, the drag at quarter-scale was larger than at full-scale. In addition, the proximity of the blade to the walls in the quarter-scale blade flume is expected to influence drag and lift characteristics.

The width of the domain of the present full-scale blade simulation was designed such that the influence of the flume walls would have minimal impact on the flow around the blade. As with the quarter-scale blade simulation, the length of the flume was set to ensure uniform bulk flow conditions at the inlet and outlet. The curved plate representing the blade was four times larger, having the same projected surface area as a standard hatchet blade, and placed in the centre of the domain. Dimensions of the full-scale model are outlined in Table 2. The boundary conditions were the same as for the quarter-scale model, except for the side walls, which were modelled as free-slip. The flume velocity was set at 2.5 m s^{-1}, which is less than the velocity used in the full-scale blade simulation (5 m s^{-1}) by Coppel et al. [13, 14], but is more representative of the average relative velocity incident on the blade throughout the stroke [15].

An unstructured tetrahedral mesh was generated, similar to that for the quarter-scale blade flume simulation. The maximum element edge length for the flow away from the blade was 10 cm, while adjacent to the blade surfaces it was 0.5 cm. A 3-mm-thick set of boundary layer cells was included on the blade surface. Grid testing indicated that this mesh, with 2.8 million elements, produced grid-independent results when compared to a 1.4 million element

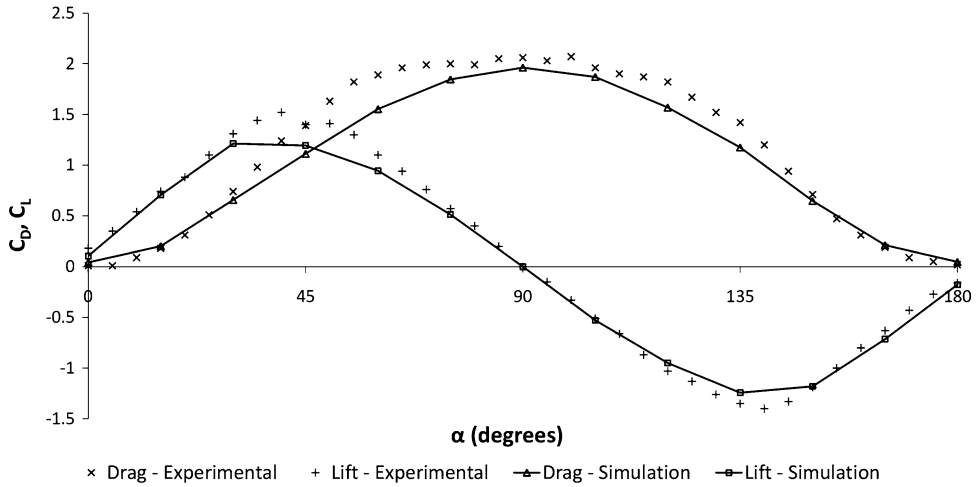

Fig. 3 Comparison of experimental and simulated drag ($C_D = F_D/0.5\rho v^2 A$) and lift coefficients ($C_L = F_L/0.5\rho v^2 A$) for a quarter-scale steady-state blade in a water flume for values of angles of attack, α. The numerical model uses the same flume dimensions, projected blade surface area, A (78.5 cm^2), and water velocity, v (0.75 m s^{-1}) as the experimental results [6]. Experimental coefficients are plotted in 5° increments as points, and the simulated coefficients are plotted in 15° increments as points connected by *straight lines*

Table 2 Dimensions of the flume and blade for the full-scale steady-state simulations

Blade	
Width	50.4 cm
Depth	25.0 cm
Projected area	1,260 cm^2
Thickness	5.0 mm
Flume	
Width	10.0 m
Length	10.0 m
Depth	1.5 m (+0.5 m of air above)

mesh. The unsteady turbulent multiphase Navier–Stokes equations (Eqs. 4–6) were solved with the SST turbulence model for α ranging from 0° to 180° in 15° increments. A 0.005 s timestep was used and the simulations were run for 5 s, allowing the monitored blade forces to reach steady-state conditions.

A comparison of drag and lift coefficients from this full-scale flow simulation with those from the modelled quarter-scale flow reveal substantial differences (Fig. 4). Although the shape of the coefficient curves is similar, the full-scale blade drag and lift values are between 20 and 30% lower than the quarter-scale values over the range of α. This difference can be attributed to several factors. The greater spacing between the blade and the flume walls in the present model are more representative of open water conditions, allowing the flow to deflect around the blade at greater distances, leading to lower drag and lift coefficients. The different Reynolds number for the two flows may also impact the values of the drag and lift coefficients.

4 Unsteady flow simulation

Quasi-static blade experiments and simulations determine drag and lift coefficients under steady conditions. They do not illustrate how these coefficients dynamically evolve in relation to the angle of attack throughout a stroke. Flow visualisation experiments on pitching airfoils show that for cases where α is increasing from 0°, the airfoil motion influences drag and lift characteristics [16]. The pitching motion of an airfoil tends to create vortices that are shed in its wake. These vortices can cause a phase lag in the absolute pressure near its trailing edge, which was shown to alter drag and lift from those found under steady-state conditions. As well, the streamlines over a pitching airfoil remain attached at values of α which would normally cause flow separation for a stationary airfoil, resulting in maximum drag and lift coefficients for a pitching airfoil exceeding those under static conditions. These behaviours suggest that the steady-state drag and lift coefficients for a rowing blade will differ from those when a blade is in motion.

To model these unsteady hydrodynamic effects, the steady model domain was modified to allow for blade motion. Like the full-scale steady model, the unsteady simulation was designed with a full-scale rectangular blade. The model accommodates blade motion by adding a cylindrical rotating domain containing the blade nested within the stationary domain of the water flume (Fig. 5). The blade is located at a radial distance from the centre of the domain equal to the outboard length of the oar (in the frame of reference of the shell, the distance from the axis of rotation of the oar to the tip of the blade). As with the full-scale steady simulation, the dimensions of the domain with

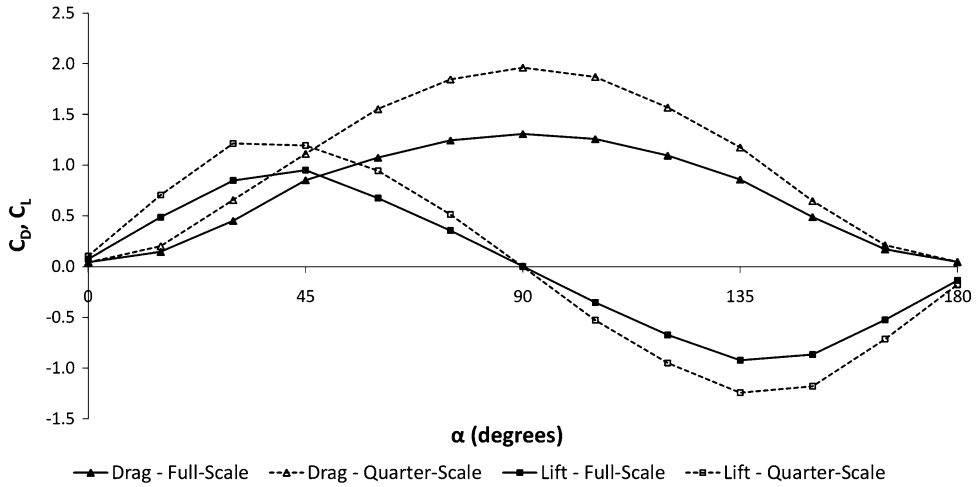

Fig. 4 Comparison of steady-state drag ($C_D = F_D/0.5\rho v^2 A$) and lift coefficients ($C_L = F_L/0.5\rho v^2 A$) for a quarter-scale blade in a water flume with a full-scale blade in open water for values of angles of attack, α. The projected surface area, A, of the quarter-scale blade is 78.5 cm^2, and the water velocity, v, is 0.75 m s^{-1}. The projected surface area, A, of the full-scale blade is 1,260 cm^2, and the water velocity, v, is 2.5 m s^{-1}. Quarter-scale blade coefficients are plotted as *open symbols* connected by *dashed lines*, and full-scale blade coefficients are plotted as *filled symbols* connected by *straight lines*

respect to the blade were tested to ensure that the proximity of the walls had a negligible effect on the flow about the blade. To account for the rotating flow within the circular domain, source terms need to be added to the streamwise and spanwise components (x- and y-components, respectively) of the momentum equation (Eq. 4). These terms model the Coriolis force, centrifugal force and an Euler force associated with a non-uniformly accelerating rotational flow,

$$S_{\text{Coriolis}} = -2\rho\omega \times U \tag{7}$$

$$S_{\text{centrifugal}} = -\rho\omega \times (\omega \times r) \tag{8}$$

$$S_{\text{Euler}} = -\rho\frac{\partial\omega}{\partial t} \times r \tag{9}$$

where U is the bulk flow velocity through the domain, ω is the angular velocity of the rotating domain, and r is the radial location from the axis of rotation. The mesh within the cylindrical domain is rigid, remaining fixed with respect to the domain motion. Specifying the instantaneous angular velocity of the rotating domain then simulates oar rotation. The varying shell velocity through the stroke is simulated by the bulk flow through the domain, flowing in the same manner as the full-scale steady model and with similar boundary conditions.

Experiments performed by Kleshnev [4] involving shells under realistic rowing conditions were able to capture data relating oar angular velocity to shell velocity during a stroke [17]. These data were also used in an analytical model developed by Atkinson which estimates the resultant shell velocity based on a variety of inputs, including oar angular velocity [18]. Using the data from Kleshnev, Atkinson's model was able to roughly replicate the resultant shell velocity observed in the experiments. This varying shell velocity, coupled with the angular velocity of the oar, is used as input in the present simulation (Fig. 6). The stroke parameters used from the experiment are outlined in Table 3.

Combining the shell liner and oar angular velocities with the known geometry of the oar (Fig. 7), a temporal variation of the nominal angle of attack, α_{nominal}, can be resolved (Fig. 8). In this figure, it is seen that α_{nominal} sweeps through nearly 190° during the relatively short stroke drive time of 0.74 s. It is noted that α_{nominal} represents the angle of incidence of flow onto the centre of the blade chord line. Since the blade is rotating, the true angle of attack will vary across the length of the blade; however, this α_{nominal} is useful in defining a reference for the relative flow on the blade.

During the stroke, the instantaneous angular velocity of the rotating domain was set to match the varying oar angular velocity based on Kleshnev's experiments. Accounting for the unsteady shell velocity, which is again based on Kleshnev's experiments, was achieved by varying the inlet flow velocity as well as adding a streamwise body force to all fluid particles in the domain. This body force, related to the shell acceleration, was applied by including a source term in the streamwise (x-component of the) momentum Equation (Eq. 4),

$$S_{\text{shell}} = \rho a_{\text{shell}} \tag{10}$$

For a multiphase flow, this approach is required because simply varying the inlet velocity over time produces unrealistic surface waves near the inlet. The motion of the shell immediately at the beginning of the stroke was

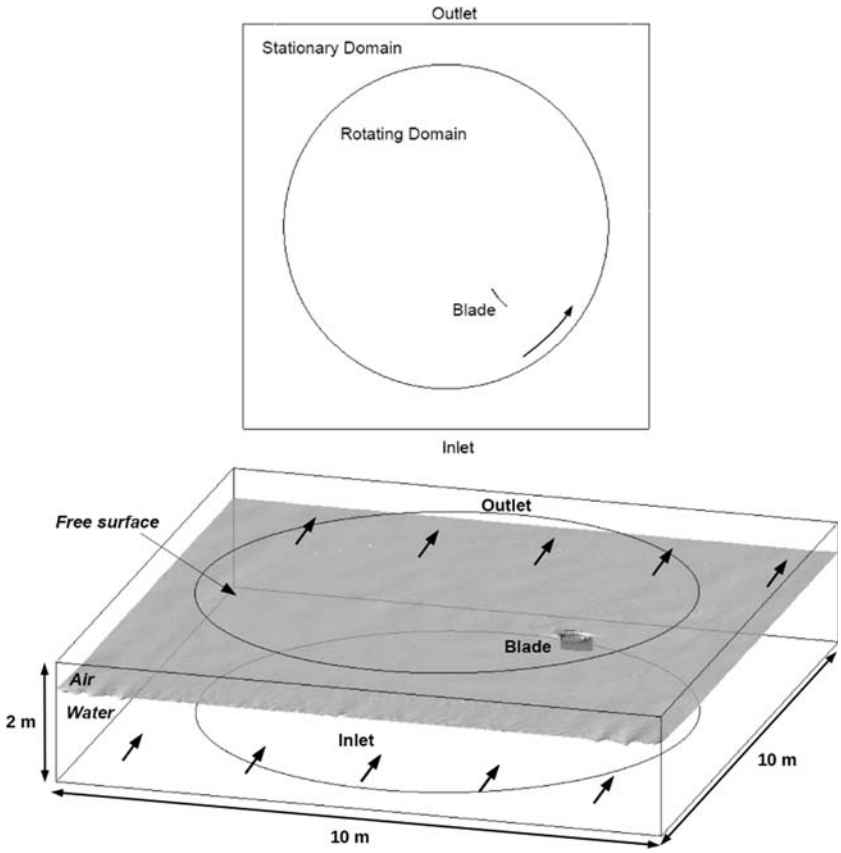

Fig. 5 Overhead and isometric views of the domain for the unsteady simulation. The inner cylindrical domain, containing the blade, rotates counterclockwise. The direction of flow through the domain, in addition to location of the free surface is indicated. The side and bottom surfaces are free-slip walls, and the top surface is a zero-pressure gradient opening

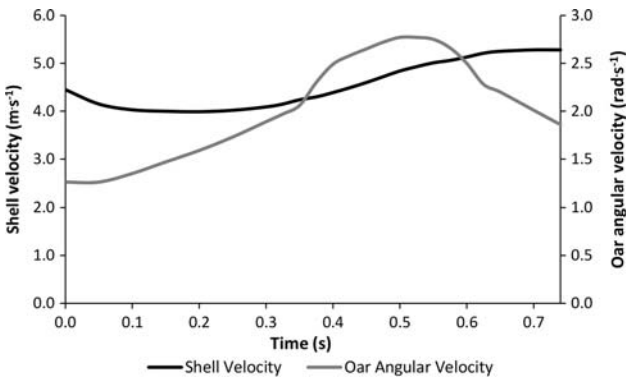

Fig. 6 Shell velocity and oar angular velocity during the stroke [17]

Table 3 Parameters of the rowing stroke [17]

Rowing stroke parameters	
Boat class	Heavy men 4
Oar outboard length	2.4 m
Stroke rate	31.1 spm
Stroke period	1.93 s
Drive period	0.74 s

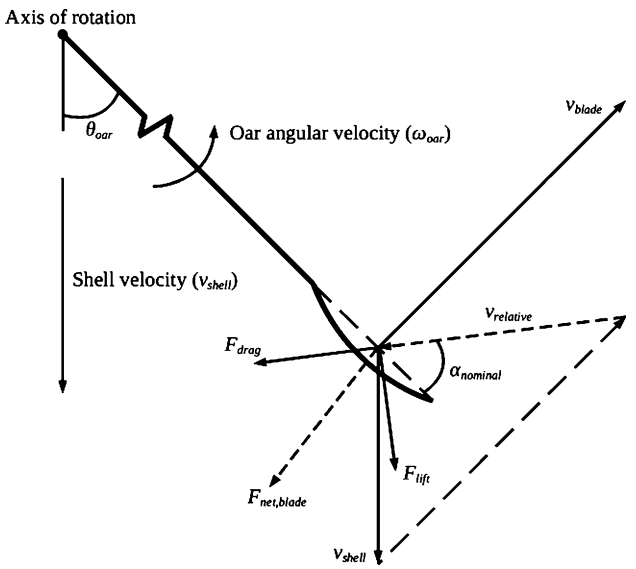

Fig. 7 View of forces on the blade and relative velocities as they relate to a blade in motion. The shell is moving downwards and the oar is rotating in a counterclockwise direction

modelled by setting the initial flow velocity within the domain to that of the shell at the catch (4.45 m s^{-1}). To simulate smooth blade entry into the water at the catch, the rotating domain was given an initial angular velocity matching the oar velocity at blade entry (1.26 rad s^{-1}). The angle of the oar to the shell centre-line (θ_{oar}) at the catch is 35°, as from Kleshnev's experiment.

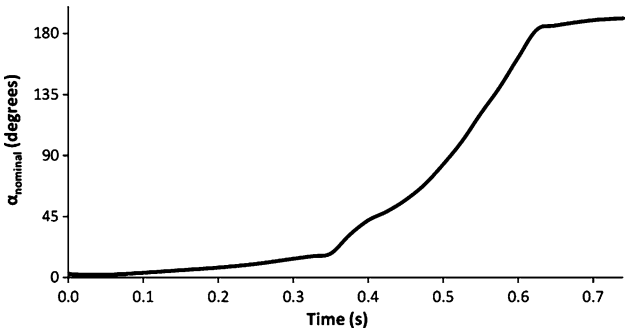

Fig. 8 Resulting temporal development of $\alpha_{nominal}$ through the duration of the stroke [17]

A similar meshing procedure to that used for the full-scale steady flow model was followed for the unsteady domain. A 2.8 million element mesh was found to provide grid-independence, and a 0.005 s timestep produced time-step-independent results. The transport equations were solved until their root mean square residuals fell below 10^{-4}. The simulation was run with the SST turbulence model, having the same turbulence intensity and length scale as the steady case, and the results are discussed in the following section.

5 Unsteady blade flow characteristics

Here, the first and most intuitively meaningful observation of the results is the evolution of the free surface around the blade. After blade insertion at the catch, there is minimal disturbance of the free surface. As the stroke progresses, there is a growing surface bulge over, and depression behind the blade (Fig. 9). At its greatest, near the end of the stroke, the bulge is approximately 10 cm high and the depression, 8 cm deep. This general surface behaviour is qualitatively very similar to what is observed in real rowing conditions.

Instantaneous streamwise and spanwise force measurements on the blade, combined with the nominal angle of attack, are used to resolve drag and lift coefficients throughout the stroke. These values are compared to those determined for the full-scale steady blade simulation over the range of $\alpha_{nominal}$ (Fig. 10).

The drag and lift coefficients produced from the unsteady simulation show a rough trend with the steady data. Through the first 0.35 s of the stroke period, $\alpha_{nominal}$ increases very slowly, staying below 15° (Fig. 8). The calculated drag and lift coefficients at these low $\alpha_{nominal}$ values are beneath those predicted from the steady simulation, remaining only slightly above zero through this stage of the stroke. This is in contrast to the steadily increasing lift and drag under steady conditions. From 0.35 to 0.6 s, $\alpha_{nominal}$ increases rapidly from 15°, becoming square to the face of the blade (90°), then further increasing to approximately 150° (analogous to 30° as seen from the shaft-side of the blade). In this range, the calculated drag and lift coefficients roughly follow the trend of the steady values. There are, however, several spurious points in this unsteady result set. At 0.375 s there is a spike in the drag and lift coefficients as $\alpha_{nominal}$ begins to rapidly increase. A 0.6 s there is an unusual behaviour of the resultant blade force, as it is directed opposite (and with a relatively high magnitude) to what is expected. The switched signs of the drag and lift coefficients are attributed to the direction of the resultant blade force vector, opposing the relative flow on the blade. From 0.625 s until the end of the stroke at 0.74 s, the flow is incident on the convex face of the blade ($\alpha_{nominal} > 180°$), for which there is no steady-state data. The low drag and lift coefficients in this region are expected, however, based on the relatively low $\alpha_{nominal}$.

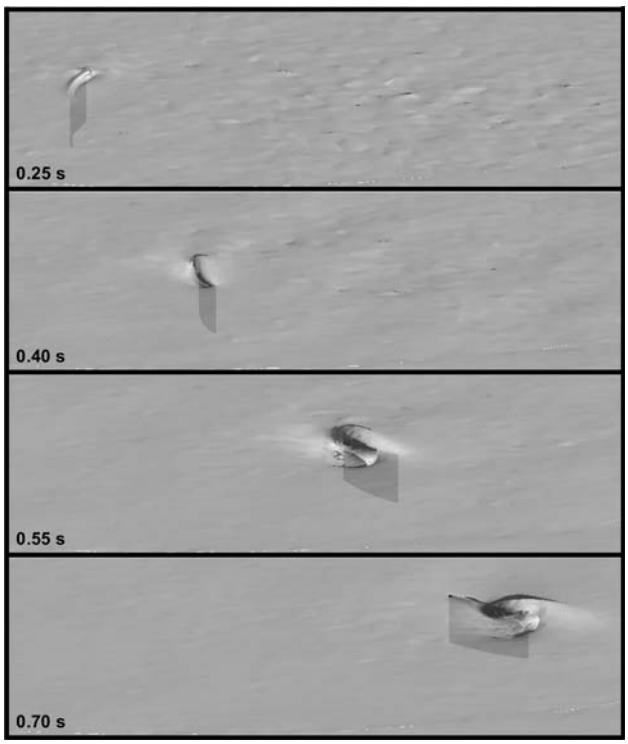

Fig. 9 Evolution of the free surface throughout the stroke. The flow is moving along with the blade sweeping from left-to-right (meaning the shell is moving from right-to-left). Near the end of the stroke there is a surface bulge of approximately 10 cm over and a depression of 8 cm behind the blade

Differences in drag and lift behaviour between the steady and unsteady flows can be attributed to a number of factors. Foremost are transient flow effects such as vortices and free surface deformations which impact the resultant force on the blade. In addition, the flow model is somewhat rigid, in that a specified shell velocity is coupled with an

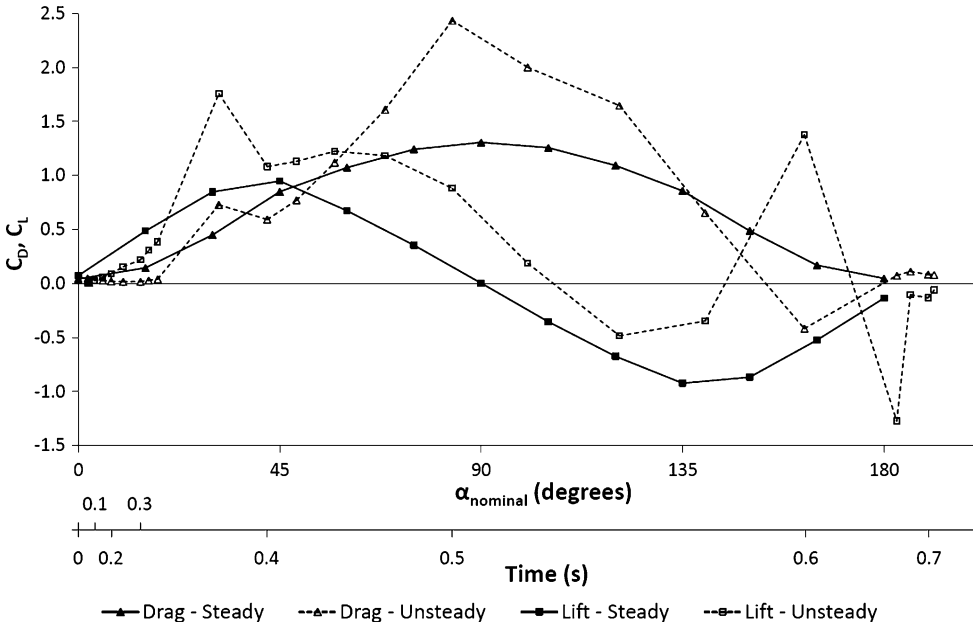

Fig. 10 Comparison of steady and unsteady drag ($C_D = F_D/0.5\rho v^2 A$) and lift coefficients ($C_L = F_L/0.5\rho v^2 A$) for a full-scale blade in open water for values of nominal angles of attack, $\alpha_{nominal}$. The projected surface area of the blade, A, is 1,260 cm^2 and v is the relative flow velocity incident on the blade. Steady-state blade coefficients are plotted as *filled symbols* connected by *straight lines*, and unsteady blade coefficients are plotted as *open symbols* connected by *dashed lines*. The time axis applies to the unsteady data

oar angular velocity. This is reasonable as they were based on experimental data obtained together, but it limits the flexibility of the model. As well, $\alpha_{nominal}$, as described before, is calculated for the midpoint of the blade chord line. Although a good static estimate of the true α on the blade chord line at an instant of time, this method does not consider the variance in α from the leading edge to the trailing edge. The drag and lift coefficients are also based on a relative flow velocity that, similar to $\alpha_{nominal}$, is a representative value for a quantity that varies across the blade chord line. The transient flow effects such as vortices and free surface deformations which impact flow on the blade are not accounted for in the nominal angle of attack and relative velocity. The growth and motion of these flow conditions are highly time dependent and can only be observed when there is a flow history. Therefore, steady blade experiments are of little applicability to a blade in motion. The flow is far too complex to be discretized into isolated segments and then pieced together in an attempt to represent a full stroke.

6 Conclusions

Steady-state quarter-scale blade drag and lift coefficients obtained from CFD modelling were found to be in excellent agreement with similar experimental flume data. A comparison with a modelled full-scale blade in a larger domain revealed that drag and lift coefficients were noticeably lower (20–30%) at full-scale compared to quarter-scale. This discrepancy is attributed to differences in Reynolds number and wall-proximity effects between the two cases. While a general trend in drag and lift coefficients with respect to α exist between the steady and unsteady cases, there are large differences, as expected.

What can be gained from this unsteady simulation is an appreciation of the difficulty in modelling the rowing stroke. This simulation affords a clear insight into the temporal development of the blade force vectors, and this information will certainly be useful in blade design. Changes can be made to allow for an optimally aligned resultant blade force throughout the stroke, as well as maximising its potential magnitude during portions of the stroke where the rower is able to apply a high force on the oar. Although the flow characteristics around a blade in motion cannot be explained solely using drag and lift coefficients, an understanding of the drag and lift mechanisms are essential when examining blade hydrodynamics.

References

1. Concept2 (2008) Choosing the right blade. http://www.concept2.com/us/oars/selection/blades/blades.asp. Accessed 28 Oct 2008
2. Macrossan MN (2008) The direction of the water force on a rowing blade and its effect on efficiency. Mechanical Engineering report no. 2008/03. University of Queensland, Australia
3. Nolte V (1993) Do you need hatchets to chop your water? Am Rowing 25(4):23–26
4. Kleshnev V (1999) Propulsive efficiency of rowing. In: Sanders RH, Gibson NR (eds) Proceedings of the XVII International Symposium on Biomechanics in Sports. Perth, Australia, pp 224–228
5. Caplan N, Gardner TN (2007) A fluid dynamic investigation of the big blade and macon oar blade designs in rowing propulsion. J Sports Sci 25(6):643–650

6. Caplan N, Gardner TN (2007) Optimization of oar blade design for improved performance in rowing. J Sports Sci 25(13):1471–1478
7. Leroyer A, Barré S, Kobus JM, Visonneau M (2008) Experimental and numerical investigations of the flow around an oar blade. J Mar Sci Technol 13:1–15
8. Hirt CW, Nicholls BD (1981) Volume of fluid (VOF) method for the dynamics of free surface boundaries. J Comput Phys 39:201–222
9. Gueyffier D, Li J, Nadim A, Scardovelli R, Zaleski S (1999) Volume-of-fluid interface tracking with smoothed surface stress methods for three-dimensional flows. J Comput Phys 152:423–456
10. Menter FR (1994) Two-equation eddy-viscosity turbulence models for engineering applications. AIAA J 32(8):1598–1605
11. Menter FR, Kuntz M, Langtry R (2003) Ten years of industrial experience with the SST turbulence model. In: Hanjalic K, Nagano Y, Tummers M (eds) Turbulence, heat and mass transfer 4. Begell House Inc, New York, pp 625–632
12. Jones WP, Launder BE (1972) The prediction of laminarization with a two-equation model of turbulence. Int J Heat Mass Transf 15:301–314
13. Coppel A, Gardner T, Caplan N, Hargreaves D (2008) Numerical modelling of the flow around rowing oar blades. In: Estivalet M, Brisson P (eds) The Engineering of Sport 7. Springer, Paris, pp 353–361
14. Coppel A, Gardner TN, Caplan N, Hargreaves DM (2009) Simulating the fluid dynamic behaviour of oar blades in competition rowing. J Sports Eng and Technol (in press)
15. Kleshnev V (2007) Rowing biomechanics newsletter (December). In: BioRow. http://www.biorow.com/RBN_en_2007_files/2007RowBiomNews12.pdf. Accessed 12 Nov 2008
16. McCroskey WJ (1982) Unsteady airfoils. Ann Rev Fluid Mech 14:285–311
17. Kleshnev V (2009) Personal communication
18. Atkinson WC (2007) Validating the ROWING model. In: Rowing computer research (or: how rowing really works). http://www.atkinsopht.com/row/validate.htm. Accessed 19 Nov 2008